optica

Dynamically reconfigurable integrated optical circulators

Duanni Huang,[1,*,†] Paolo Pintus,[1,2,†] Chong Zhang,[1] Paul Morton,[3] Yuya Shoji,[4] Tetsuya Mizumoto,[4] and John E. Bowers[1]

[1]Electrical and Computer Engineering Department, University of California Santa Barbara, California 93106, USA
[2]Scuola Superiore Sant'Anna, via Moruzzi 1, 56124 Pisa, Italy
[3]Morton Photonics, 3301 Velvet Valley Dr, West Friendship, Maryland 21794, USA
[4]Department of Electrical and Electronic Engineering/FIRST, Tokyo Institute of Technology, Tokyo, Japan
*Corresponding author: duanni@umail.ucsb.edu

Received 16 September 2016; revised 16 November 2016; accepted 29 November 2016 (Doc. ID 275809); published 21 December 2016

Optical circulators that unidirectionally route light could lead to bidirectional operations in applications in data centers and telecommunications, as well as sensors. In this work, to the best of our knowledge, we present the first realization of integrated optical circulators on silicon that are electrically driven and dynamically reconfigurable. The proposed device utilizes silicon microrings with a bonded magneto-optic cladding alongside an integrated electromagnet for nonreciprocal behavior. This novel approach does not use a permanent magnet and, for this reason, it is more attractive for packaging and further integration with lasers and other photonic devices. We use this device architecture to demonstrate 4- and 6-port optical circulators with up to 14.4 dB of isolation and propose a framework to extend the design to an arbitrary number of ports. Finally, we demonstrate that it is possible to switch the electromagnet and reconfigure the circulator on a sub-nanosecond timescale, potentially adding a new level of device functionality.

OCIS codes: (230.3240) Isolators; (230.3810) Magneto-optic systems; (230.5750) Resonators; (130.3120) Integrated optics devices.

https://doi.org/10.1364/OPTICA.4.000023

1. INTRODUCTION

Optical isolators and circulators are nonreciprocal devices that allow for the unidirectional propagation of light [1]. Optical isolators are two-port devices that serve as a one-way street for photons and are crucial in preventing undesired back-reflections from interacting with a laser. Expanding on this analogy, optical circulators are many-port devices that act as a roundabout for photons, with each input port routed to exactly one output port in a nonreciprocal fashion. Integrated circulators would enable bidirectional operations in optical interconnects [2–4], which could double the network capacity in many data center and telecommunication applications [5]. They are also important components in many distributed fiber sensors and other interferometric optical sensors [6].

Achieving the necessary optical nonreciprocity on chip is a challenging task, and various approaches have been investigated using spatial-temporal, electro-optic-based modulation [7–13], as well as optical nonlinearities such as stimulated Brillouin scattering [14,15]. Thermo-optic and Kerr-like nonlinearities have also been used to make optical diodes [16,17], although dynamic reciprocity may prevent them from functioning as isolators [18]. While these methods are attractive since they only require Si or III–V materials, they rely on fairly weak effects and have been limited in isolation or intrinsically have high losses. In some cases, they also require multiple modulators with high-speed electronic drive signals and additional optical filters, which can significantly increase the footprint and complexity of the device [12,13].

On the other hand, the magneto-optic Faraday effect provides a simple, straightforward path toward nonreciprocity and is widely used in fiber and bulk-optic circulators today. However, the transition to integrated photonics has been challenging due to severe lattice and thermal mismatch between commonly used magneto-optic materials, such as cerium-substituted yttrium iron garnet (Ce:YIG) and Si or III–V substrates [19]. Recently, there have been several works that investigated pulsed laser deposition or sputtering of magneto-optic garnets on silicon [20–23]. While these methods show great promise as a monolithic technology, they require the presence of a virtual substrate or buffer layer, as well as a high-temperature, rapid thermal anneal (>700°C) to promote the crystallization of the magneto-optic garnets. An alternate approach to integrating magneto-optic garnets onto silicon substrates is heterogeneous integration using wafer bonding techniques, which can circumvent the lattice mismatch issue [24]. Heterogeneous integration has been used to integrate vastly different materials, including III–V's, $LiNbO_3$, and Ce:YIG on silicon-on-insulator (SOI) substrates in order to obtain optical gain and efficient nonlinear effects, as well as the desired optical nonreciprocity for silicon photonics [25,26]. In this approach, the

magneto-optic material (Ce:YIG) is grown on a lattice matched (Ca, Mg, Zr) -substituted gadolinium gallium garnet (SGGG) substrate and then bonded on silicon waveguides. Several isolators and circulators have been demonstrated with this approach [27–35], which does not require a high temperature anneal and is compatible with multiple die bonding techniques for high-performance photonic-integrated circuits.

In this paper, we demonstrate heterogeneously integrated optical circulators on silicon operating in the transverse magnetic (TM) mode with up to 14.4 dB of isolation ratio. Unlike previous integrated circulators that utilize an asymmetric Mach–Zehnder interferometer (MZI) structure [28–32], we exploit a microring-based structure with a significantly reduced footprint (20 μm radius). Furthermore, we do not use a permanent magnet to generate the magnetic field. Instead, a localized magnetic field is generated from an integrated microstrip that serves as an electromagnet and can be tailored to match various device geometries. This current-induced magnetic field can be switched with a rise and fall time of 400 ps, which flips the direction of the magnetic field and reroutes all the optical pathways in the device. Thus, the circulator can be dynamically reconfigured on a sub-nanosecond timescale. Finally, we demonstrate that this design for a 4-port circulator can be cascaded to realize a 6-port circulator with four different working configurations. We can achieve an arbitrary number of ports by expanding this device architecture even further, which may lead to novel reconfigurable optical networks and switches on-chip.

2. DEVICE OVERVIEW

A variety of optical isolators and circulators have been demonstrated based on different magneto-optic related phenomenon, ranging from TE–TM mode conversion to nonreciprocal loss and phase shift. Of all these approaches, the nonreciprocal phase shift (NRPS) effect has been the most widely used of late, as it does not require the tight fabrication accuracy necessary for phase matching in mode conversion. A nonreciprocal phase shift is a first-order effect that occurs when light flows through a magneto-optic medium that is magnetized perpendicular to the direction of light propagation, also known as the Voigt configuration. Depending on whether the magnetic field is in-plane or out-of-plane with respect to the waveguide, NRPS is achieved for the TM and TE modes, respectively [35]. In the TM case, the magneto-optic material serves as a top cladding (or bottom cladding) for the waveguide, while the magnetic field is in-plane and transverse to the light propagation direction. Under these circumstances, the propagation constants of the forward (β^+) and backward (β^-) propagating light in the waveguide are different. The sign of the difference in the propagation constant ($\Delta\beta = \beta^+ - \beta^-$) is dependent on the direction of magnetization with respect to the propagation. Therefore, if the magnetization direction is flipped, we obtain the opposite sign on $\Delta\beta$, as if β^+ and β^- are interchanged due to a change in the propagation direction. This is the operating principle behind reconfigurability in this work. Isolation for the TE mode can be achieved by using a polarization rotator before the TM mode isolator [33] or by achieving a structure in which the magneto-optic material is laterally adjacent to the waveguide [35].

In order to achieve optical isolation and circulation based on the NRPS, a phase-sensitive structure, such as an MZI or a microring, is needed. Previous experiments have shown high optical isolation as well as successful circulation using an asymmetric MZI in which there is a $\pm\pi/2$ NRPS on one arm according to the direction of propagation, such that it interferes constructively (forward) and destructively (backward) with the reciprocal arm, which is set at a phase bias of $2m\pi + \pi/2$. Depending on the integer value of m, the free spectral range (FSR) of the MZI can be adjusted, and thus, the 20 dB bandwidth can be set to be as wide as 8 nm [28]. A disadvantage of this device is an enlarged footprint, since the length of magneto-optic interaction in the waveguide required for $\pi/2$ NRPS is typically hundreds of microns [30] to several millimeters long [33], depending on the exact waveguide geometry. On the other hand, a miniaturized footprint is one of the main reasons the ring resonator has been so widely studied over the past decade. This footprint reduction plays an especially important role in magneto-optic devices due to the lossy nature of Ce:YIG (~40–60 dB/cm) [19,28] and other magneto-optic materials, such as cobalt ferrites (~dB/μm) [36]. Thus, a microring structure has great potential to reduce the insertion loss of the device by reducing the footprint. We have previously demonstrated this concept in a microring isolator with 32 dB of isolation and only 2.3 dB of excess loss to silicon [37,38]. Microrings come with an inherent drawback of limited bandwidth. However, this may be improved with the design of coupled or cascaded ring filters.

In a microring isolator or circulator, the magneto-optic Ce:YIG serves as an upper cladding over the ring, and the applied magnetic field must be either radially inward or outward with respect to the ring in order to achieve NRPS for the TM mode. The difference in propagation constants causes a resonance wavelength split between the clockwise (CW) and counterclockwise (CCW) modes in the resonator. The magnitude of this resonance wavelength split (RWS) is dependent on the strength of the magnetic field below magnetic saturation, as well as the waveguide geometry. For an optical circulator, we utilize the microring in an add–drop filter configuration, as shown below, in Fig. 1. Here, we have shown the two scenarios where the magnetic field is pointing radially inward (top) or outward (bottom). The port that is used as the input will determine the propagation direction of light and therefore whether we couple to the CW or CCW mode in the ring.

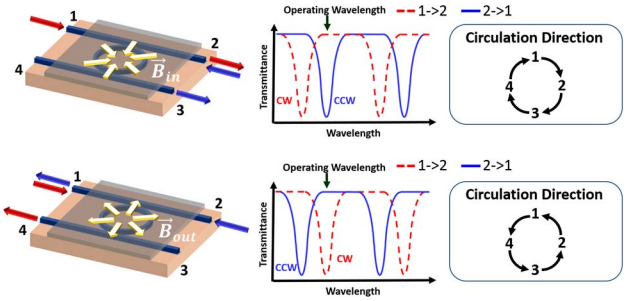

Fig. 1. We depict the spectrum of the through port of the ring for the two operating configurations of the circulator. Light entering from port 1 will couple into the CW mode (the transmittance spectrum is plotted in the red dashed line) and light entering from port 2 will couple into the CCW mode (the transmittance spectrum is plotted in the blue continuous line). For the sake of simplicity, we do not depict the transmittance spectrum at the drop port, as it can be assumed to have the same resonant characteristics. By flipping the magnetic field, the circulation is reversed at the same operating wavelength.

In Fig. 1, we align the operating wavelength to the CCW resonance of the ring. Under these conditions, the wavelength of light entering from port 1 (red arrow) is not aligned with the ring resonance, and therefore, the light passes through to port 2. Meanwhile, light injected from port 2 (blue arrow) excites the CW ring resonance, and it will be dropped to port 3. Thus, the circulation direction in this configuration is $1 \rightarrow 2 \rightarrow 3 \rightarrow 4 \rightarrow 1$. If the magnetic field is flipped to a radially outward direction, as shown in the bottom half of Fig. 1, the same operating wavelength is now aligned to the CW resonance. In this alternate configuration, the light circulates from $1 \rightarrow 4 \rightarrow 3 \rightarrow 2 \rightarrow 1$. As long as the magnetic field can be reliably switched, the circulator can be reconfigured. This equivalence between switching the propagation direction and switching the current direction is confirmed in the Supplement 1.

Conventionally, isolators and circulators are packaged with small, permanent magnets (~mm^2 to cm^2) that provide the necessary magnetization of the material. However, it is difficult to generate radially orientated magnetic fields over a small microring using permanent magnets and even more difficult to switch the magnetization. Special care must also be taken in the packaging of these magnets, and they remain a discrete component in an otherwise fully integrated device. There has been prior research involving the use of thin-film permanent magnets for optical isolators [39], but this does not address the issue of generating a radial magnetic field. Instead, we use an integrated metallic microstrip that is on top of the garnet cladding, which serves as an electromagnet. The current applied through this microstrip will generate a local magnetic field in the magneto-optic material (i.e., the waveguide top cladding) and can be easily switched to realize the aforementioned reconfigurability. The microstrip can follow the shape of any waveguide structure, whether it is the microring shown here or an MZI device, and it can be designed to provide the desired magnetic field profile. Finally, this approach is much more suitable for packaging and co-integration with integrated electronic circuits and drivers.

3. DEVICE DESIGN AND FABRICATION

The ring resonator is designed with a cross section that optimizes the RWS under a transverse magnetic field, while maintaining single-mode operation for TM modes [40]. For the optimization, we use a finite element nonreciprocal mode solver to accurately calculate the NRPS for a given waveguide geometry [41]. The 4-port circulator in this paper consists of an add–drop ring resonator filter with a radius of 20 μm and is depicted below in Fig. 2(a). The ring radius is chosen to avoid bending loss, as the optical confinement in the silicon is lower due to the presence of a magneto-optic garnet cladding, as shown in Fig. 2(b). The resonator is fabricated on a silicon-on-insulator (SOI) wafer using DUV lithography, and then the Ce:YIG ($n = 2.2$) on SGGG ($n = 1.97$) die is directly bonded on top of the microring using an O_2 plasma assisted bonding process. The bond is annealed at 200°C under 3 MPa of pressure to strengthen the bond. Next, the backside of the bonded die is thinned down to roughly 8 μm using mechanical polishing. Finally, the integrated electromagnet is fabricated by depositing a 1.5 μm thick gold microstrip on the backside of the bonded die, as depicted in the microscope image in Fig. 2(c).

The input/output relation of the 4-port device can be effectively described by the scattering matrix

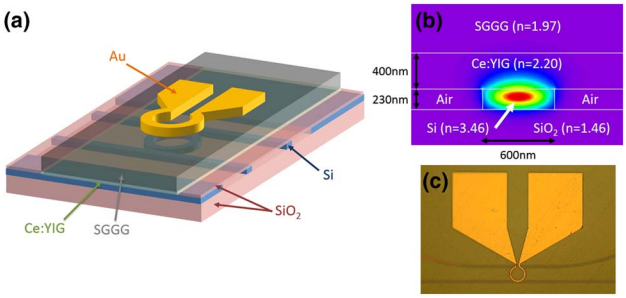

Fig. 2. (a) 3D prospective view of the device, (b) cross-sectional mode profile, and (c) microscope image of the fabricated device. The silicon waveguide is 230 nm tall and 600 nm wide, and the Ce:YIG is 400 nm thick. A thin layer of silica (~10 nm) is assumed to have formed between the waveguide and the bonded layer due to the plasma activation [24].

$$\begin{pmatrix} A_1^- \\ A_2^- \\ A_3^- \\ A_4^- \end{pmatrix} = \begin{pmatrix} 0 & S_{12} & 0 & S_{14} \\ S_{21} & 0 & S_{23} & 0 \\ 0 & S_{32} & 0 & S_{34} \\ S_{41} & 0 & S_{43} & 0 \end{pmatrix} \begin{pmatrix} A_1^+ \\ A_2^+ \\ A_3^+ \\ A_4^+ \end{pmatrix}, \tag{1}$$

where A_i^- (for $I = 1, 2, 3, 4$) represents the amplitude of the output light, and A_j^+ (for $j = 1, 2, 3, 4$) is the amplitude of the input light. We assume that the backscattering caused by the waveguide roughness is negligible, so the scattering coefficients along the diagonal are set equal to zero. For the same reason, the light injected from port 1 can only propagate through port 2 and port 4 but not to port 3, which implies $S_{31} = 0$. With similar arguments, $S_{24} = S_{13} = S_{42} = 0$. Moreover, if the two waveguides have symmetric coupling with the microring, the following identity is held, and only four scattering coefficients are needed:

$$S_{12} = S_{34}, \qquad S_{14} = S_{32}, \qquad S_{41} = S_{23}, \qquad S_{43} = S_{21}. \tag{2}$$

It is worth noting that the scattering matrix is asymmetric due to nonreciprocity and $S_{ij}(\lambda) \neq S_{ji}(\lambda)$. Instead, the spectra for the nonzero coefficients are related by the following relation,

$$S_{ij}(\lambda \pm \Delta\lambda_{MO}/2) = S_{ji}(\lambda \mp \Delta\lambda_{MO}/2), \tag{3}$$

where $\Delta\lambda_{MO}$ is the resonance wavelength split in the ring, and the sign in the argument must be chosen according to the direction of the external magnetic field. As with any microring, a key parameter in determining the scattering matrix is the waveguide ring coupling power (K). In our design, we have fixed K to be 10.45%, in order to achieve equal isolation ratios among all the ports, which is described in more detail in the Supplement 1.

As described in Fig. 2, a gold microstrip coil was deposited to serve as the electromagnet. In order to provide a large magnetic field while limiting heating, a large current and a small resistance are required. Therefore, the gold microstrip cross section is set to be 3 μm wide and 1.5 μm thick, with a measured resistivity near 1 Ohm. Simulations using COMSOL multiphysics for magnetic and thermal properties are shown in Fig. 3. The plots depict the radial component of the magnetic field (H_r) in the CeYIG layer above the ring and the average temperature increment (ΔT) in the silicon ring as a function of the current in the coil. As we expected, the field H_r varies linearly with the current, while ΔT is a quadratic function of the current due to the Joule effect.

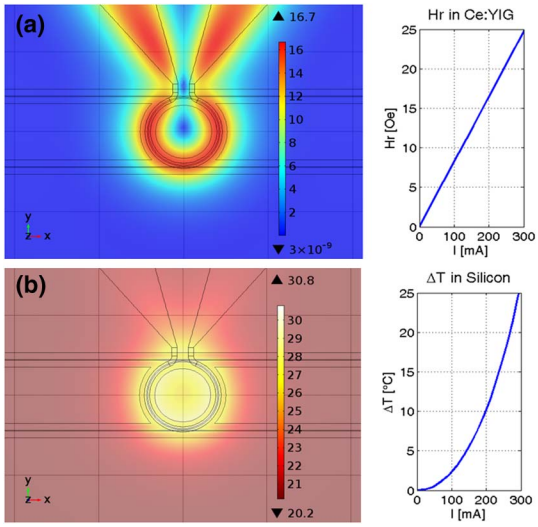

Fig. 3. (a) Radial magnetic field map (in Oersted) in the Ce:YIG layer for an injected current $I = 200$ mA ($V = 190$ mV), as well as its linear dependence with the injected current. (b) Temperature variation (in Celsius) in the silicon layer for an injected current $I = 200$ mA, and its quadratic dependence with the injected current. For the device under test, a current of 200 mA provides a radial magnetic field of about 17 Oe in the Ce:YIG layer, while the temperature increment is about 10°C in the silicon microring.

These simulations are key to understanding the behavior of the circulator at different driving currents.

4. EXPERIMENTAL RESULTS

We characterize the device at room temperature (20°C) using a polarization-maintaining (PM) lensed fiber to inject TM-polarized light. Then, we measure the transmittance spectra through the device at the output ports when we apply −200 mA of current through the microstrip. This corresponds to roughly 40 mW of dissipated power in the microstrip. This may be improved by using a larger gold cross section, thinning the SGGG further, or depositing multiple coils of the electromagnet. Further details on the experimental setup can be found in the Supplement 1. The experimental results are shown in Fig. 4(a), where all the spectra have been normalized to a reference silicon waveguide of the same dimension but covered by a silica top cladding instead of the Ce:YIG. For comparison, the simulated spectra are reported in Fig. 4(b). The simulated and measured scattering coefficients exhibit a good agreement between the theory and the experiments, confirming the validity of our model.

Because the bonded chip is 3.5 mm long, the propagation loss in the input/output waveguide is estimated to be 8.7 dB due to the absorption of the Ce:YIG (∼40–60 dB/cm), where the mode overlap is computed to be about 41%. The measured wavelength split between the CW (red) and CCW (blue) resonances in Fig. 4(a) is measured to be 0.35 nm. This value is smaller than the simulated maximum of 0.55 nm because the magnetic field is below the saturation value for the Faraday rotation (i.e., 50 Oe) as well as a temperature-induced reduction of the magneto-optic effect [38,42]. In Fig. 5, the nonreciprocal resonance split (MO) and the reciprocal shift (Therm.) are shown as functions of the injected current. The values predicted by our model and the measured ones show a very good agreement between the theory and the experiments.

If we choose to operate near $\lambda = 1558.45$ nm, denoted by the dashed black line in Fig. 4(a), then the light in the device circulates from $1 \to 2 \to 3 \to 4 \to 1$. From these measurements, we are able to summarize the performance of the 4-port circulator as shown in Table 1, where the amplitudes of the scattering coefficients are reported at the working wavelength. The missing entries are paths that are only obtainable due to strong back-reflections. We were unable to quantitatively measure the values of S_{13}, S_{31}, S_{24}, and S_{42}, as they are very low (less than −40 dB). Likewise, the measurement to quantify the backscattered light at each port (S_{ii}, for $I = 1, 2, 3, 4$) is dominated by reflections off the polished facet as well as the lensed fiber used for the coupling.

In this table, the highlighted entries depict the insertion loss for the forward circulating path and range from 9.7 to 12.4 dB. Such large values are due to the Ce:YIG clad bus waveguides

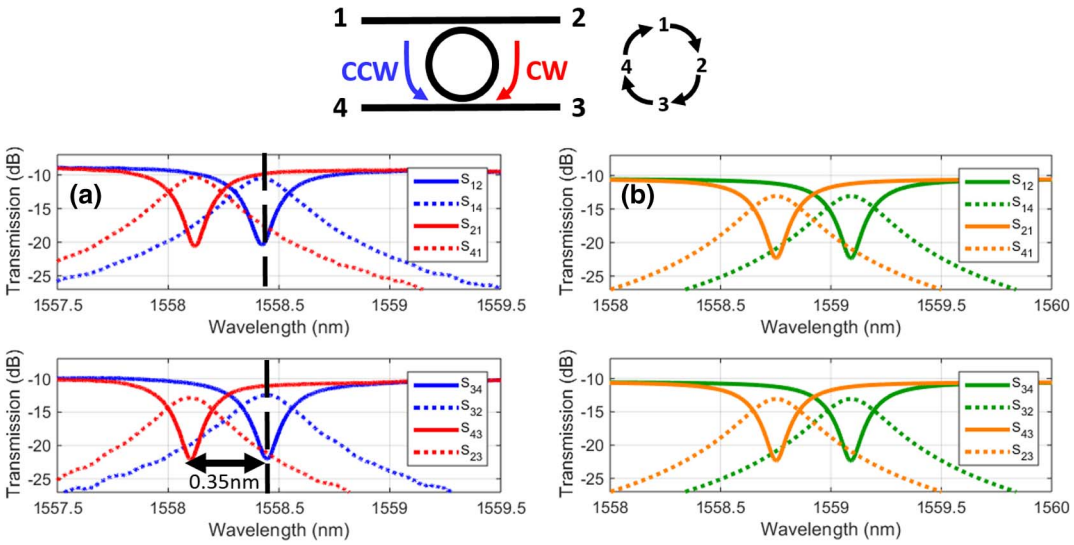

Fig. 4. (a) Measured and (b) simulated transmission spectra of the CW and CCW resonances at the through and drop ports. The curves are labeled by the corresponding entry in the scattering matrix. Due to fabrication inaccuracies in the waveguide, the measured spectra are shifted with respect to the measured ones. The thermal heating can be effectively used to control the resonance position, compensating the variation of the waveguide cross-section size.

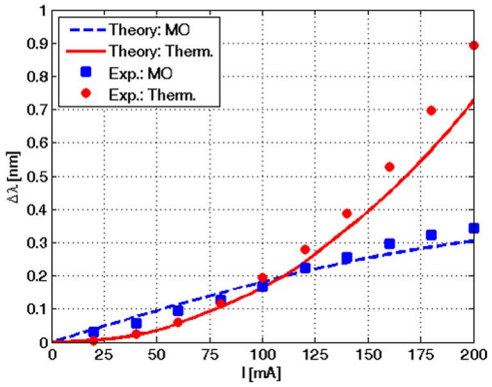

Fig. 5. Measured and predicted reciprocal resonance shift (thermal effect) and nonreciprocal resonance split (MO effect) have been reported as a function of the applied current.

Table 1. Experimental Transmittance Data [dB] of the Circulator at the Working Wavelength of $\lambda = 1558.45$ nm

		Input Port			
		1	**2**	**3**	**4**
Output Port	**1**	–	−20.7	–	**−10.5**
	2	**−9.7**	–	−21.0	–
	3	–	**−12.4**	–	−22.0
	4	−17.2	–	**−11.0**	–

(3.5 mm), which are much longer than the actual microring size (i.e., 20 μm radius) and can be reduced by shrinking the die size or using transitions to push the mode away from the Ce:YIG. We do not notice any increase in the insertion loss due to the magnetic field or heating of the device.

As formerly stated, the isolation ratio is defined as the ratio of forward to backward transmitted power between two adjacent ports. The largest isolation ratio is 11 dB, and it is measured between port 1 and port 2, and between port 3 and port 4 (i.e., IR_{12} and IR_{34}). Vice versa, the smallest isolation ratio is 6.7 dB that is measured between port 1 and port 4 (i.e., IR_{14}). Another important key feature to evaluate the performance of the device is the crosstalk at the output port (XT). It can be defined as the ratio between the sum of transmitted signal powers from all undesired ports and the transmitted signal power from the desired output port. From Table 1, it is calculated as the difference between the entries in any horizontal row. The crosstalk in this device ranges from −6.2 dB at port 4 to −11.3 dB at port 2. The results are summarized below in Table 2. The measured IRs are smaller than the simulated values because the device is operating below the saturation magnetization value ($\Delta\lambda_{MO} < 0.55$ nm), as shown in the table.

Both the isolation ratio and the crosstalk of the device can be improved by increasing the RWS and differentiating the CW and CCW resonance even further. However, more current is needed, and that can produce larger heating and eventually damage the device. To avoid this issue, we plan to use multiple coils for the electromagnet, allowing for higher magnetic fields at a lower operating current and temperature [43].

We also investigate the switching time of the device, or the time it takes to reconfigure the circulator. The wavelength is set to bias the ring at the side of the resonance for higher modulation

Table 2. Simulated and Experimental Isolation Ratio and Crosstalk[a] at the Working Wavelength of $\lambda = 1558.45$ nm for Different Values of $\Delta\lambda_{MO}$ [nm]

	$\Delta\lambda_{MO} = 0.55$ (Simulated)	$\Delta\lambda_{MO} = 0.35$ (Simulated)	$\Delta\lambda_{MO} = 0.35$ (Experiment)
$IR_{12} = \lvert S_{21}\rvert^2/\lvert S_{12}\rvert^2$	12.0 dB	11.6 dB	11.0 dB
$IR_{23} = \lvert S_{32}\rvert^2/\lvert S_{23}\rvert^2$	12.0 dB	8.5 dB	8.6 dB
$IR_{34} = \lvert S_{43}\rvert^2/\lvert S_{34}\rvert^2$	12.0 dB	11.6 dB	11.0 dB
$IR_{41} = \lvert S_{14}\rvert^2/\lvert S_{41}\rvert^2$	12.0 dB	8.5 dB	6.7 dB
$XT_1 = \lvert S_{12}\rvert^2/\lvert S_{14}\rvert^2$	−14.3 dB	−10.18 dB	−10.2 dB
$XT_2 = \lvert S_{23}\rvert^2/\lvert S_{21}\rvert^2$	−10.0 dB	−10.0 dB	−11.3 dB
$XT_3 = \lvert S_{34}\rvert^2/\lvert S_{32}\rvert^2$	−14.3 dB	−10.18 dB	−9.6 dB
$XT_4 = \lvert S_{41}\rvert^2/\lvert S_{43}\rvert^2$	−10.0 dB	−10.0 dB	−6.2 dB

[a]The crosstalk is calculated assuming equal input powers at each port.

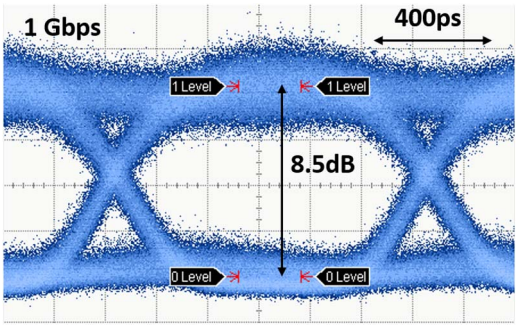

Fig. 6. Magneto-optic rise time of the device is measured to be 400 ps using a 1 Gbps PRBS31 bit stream. The eye stays open up to 2.5 Gbps, which agrees well with the measured rise time.

efficiency, and the input is a zero-mean signal such that the temperature remains constant for the device. To test the rise time of the magneto-optic response, a pseudo-random bit sequence (PRBS31) with 1.5 Vpp and no DC bias is applied to the electromagnet, while an optical signal is injected from port 1 and the output light at port 2 is collected on a sampling oscilloscope. For a PRBS at 1 Gbps, the resulting eye diagram is shown in Fig. 6, where we measure a 400 ps rise time with an 8.5 dB extinction ratio.

In this experiment, the magneto-optic response is limited by the rising impedance of the electromagnet at higher frequencies, which acts as an inductor. Nevertheless, it is significantly faster than the slow thermal-controlled microrings that are being utilized for large-scale photonic switching fabrics [44]. Faster operation can be achieved by reducing skin depth effects and lowering the inductance of the microstrip, although additional limitations caused by magnetization reversal (~2 ps) [45] and photon lifetime (~12 ps) in the ring will eventually become relevant.

5. MULTIPLE PORT (>4) CIRCULATORS

The demonstrated 4-port circulator can be used as a building block for more complex nonreciprocal devices and networks. Here, we demonstrate how our device design can be expanded to realize circulators with an arbitrary number of input/output ports. We will only consider devices using the microring architecture; nevertheless, the principles shown here can be carried over to design multi-port MZI circulators as well. In this section,

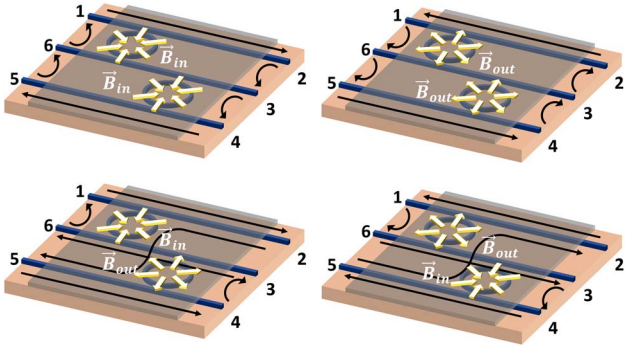

Fig. 7. Four possible configurations of the proposed 6-port circulator. The white arrows show the radially inward or outward magnetic field, while the black arrows show the circulation direction of light for each configuration.

we present, for the first time, to the best of our knowledge, a fully circulating, dynamically reconfigurable 6-port optical circulator with up to 14.4 dB of isolation.

The simplest design for a multi-port microring circulator involves a single central ring with multiple bus waveguides. While the simplicity in only using one ring is attractive, the optical crosstalk between the ports would likely be a critical issue due to the recirculation of the signal in the central ring [46]. Moreover, the footprint will enlarge with an increasing number of ports. An alternate design we present here uses multiple rings laid out in the geometry depicted below. Figure 7 shows the schematic for a 6-port circulator using two identical rings and three bus waveguides. The top two configurations show both fields inward or outward and circulation paths of $1 \rightarrow 2 \rightarrow 3 \rightarrow 4 \rightarrow 5 \rightarrow 6 \rightarrow 1$ and $1 \rightarrow 6 \rightarrow 5 \rightarrow 4 \rightarrow 3 \rightarrow 2 \rightarrow 1$, respectively. In the bottom two configurations, the magnetic fields in the two rings are in opposite directions. Under these circumstances, the circulation path is $1 \rightarrow 6 \rightarrow 3 \rightarrow 4 \rightarrow 5 \rightarrow 2 \rightarrow 1$ for the case in the bottom left and for the bottom right. In general, this multi-port architecture can be easily expanded to an arbitrary number of ports. If we use $(N-1)$ rings with (N) bus waveguides, we are able to achieve a circulator with $(2N)$ ports. Odd numbers of ports can be realized by using a loop mirror

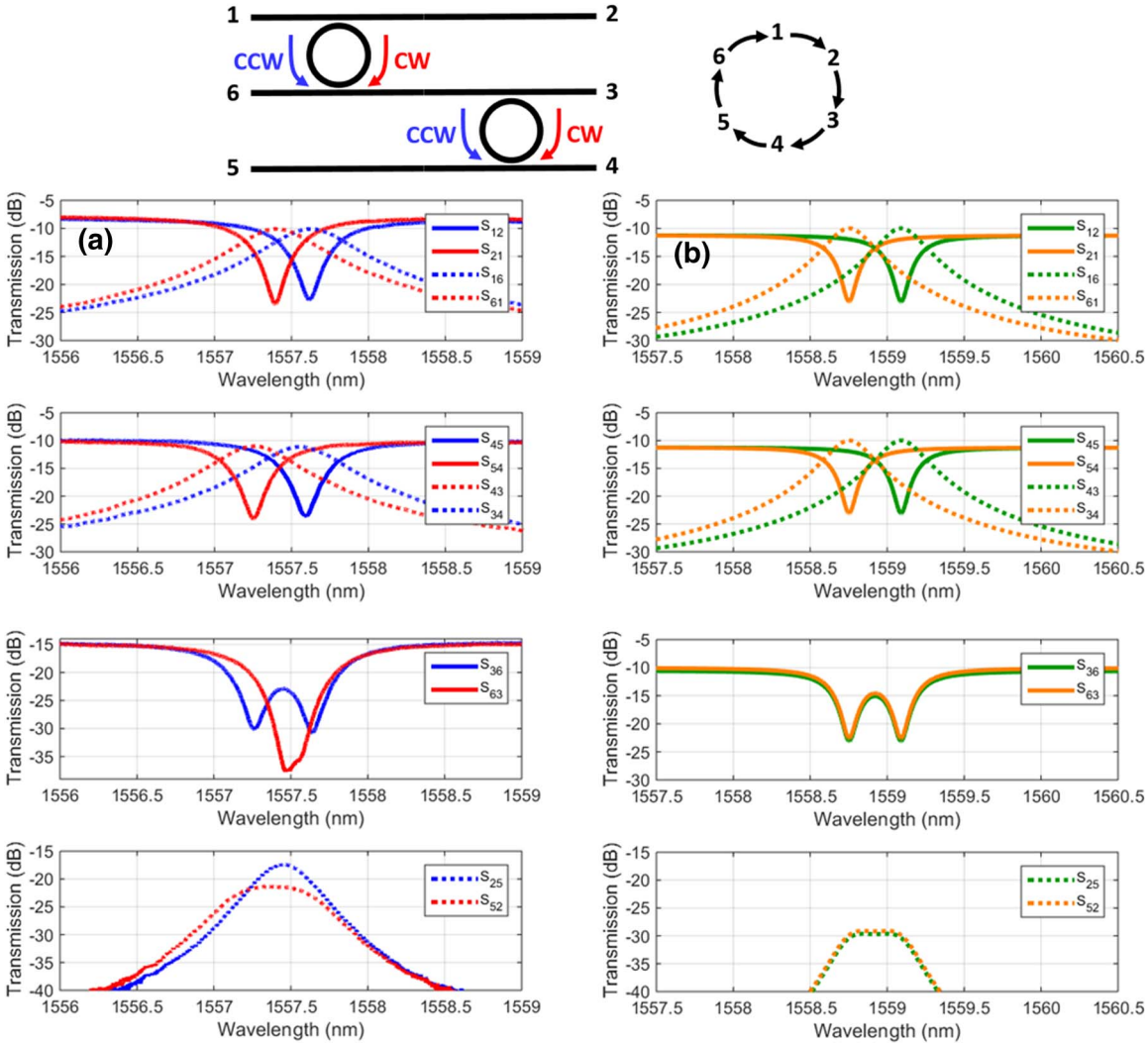

Fig. 8. (a) Measured and (b) simulated transmission spectra of the 6-port circulator. The deviations between the two are largely due to fabrication imperfections in the ring, which leads to a different driving current in the two rings in order to align the resonances. In addition, the experimental spectra S_{61}, S_{16}, S_{34}, and S_{43} show a much larger bandwidth, which is due to a larger than expected coupling coefficient ($K > 10.45\%$), which is most likely due to a smaller than desired ring-waveguide coupling gap.

at the end of one of the bus waveguides, as was previously demonstrated with a 3-port circulator [32].

As long the rings are separated far enough such that the magnetic field in one ring does not significantly affect the others, then we can magneto-optically tune the $(N-1)$ rings independently and reconfigure the circulator in $2(N-1)$ ways. For a 6-port circulator, it is possible to obtain the four different configurations shown above, depending on the orientation of the magnetic field in the two rings. We fabricated this 6-port optical circulator using two 20 μm ring resonators and three bus waveguides. In theory, the rings should be identical with the same resonance wavelength, but this is often not the case due to fabrication imperfections and nonuniformities of the wafer or the etch process. Our result shows the intrinsic resonances of the two rings are over 1 nm apart, meaning they must be thermally tuned together in order for the circulator to operate at a common wavelength for all of the ports. Furthermore, we must apply enough current to observe a significant RWS in each of the rings for nonreciprocal behavior.

In this design, the single microstrip can be used to meet both of the aforementioned requirements for single wavelength circulation and compensate for the fabrication. Applying a different current in each ring, we found that the optimal conditions for 6-port circulation in the device under test are $I_1 = \pm 185$ mA for the top ring and $I_2 = \pm 262$ mA for the bottom ring. Due to the angling of the output facets and limited spacing between adjacent facets, it was not possible to simultaneously test all input and output combinations. Instead, we use each of the six ports as an input successively and measure the transmission spectra through all the accessible output ports, as shown in Fig. 8. Further details can be found in the Supplement 1.

Although the predicted RWS is 0.35 nm, from the measured spectra we observe a RWS of 0.25 nm for the top ring while the RWS of the bottom one is 0.35 nm, as shown in Fig. 8. This is reasonable considering the applied current was larger for the bottom ring in order to compensate the fabrication variation. In this configuration, the operating wavelength near 1557.6 nm is on resonance with the CCW modes of both rings, causing a circulation path of $1 \rightarrow 2 \rightarrow 3 \rightarrow 4 \rightarrow 5 \rightarrow 6 \rightarrow 1$. From these measurements we can extract the scattering parameters of the device at the working wavelength in Table 3. Once again, the highlighted entries show the insertion loss along the forward circulation path, and the isolation and crosstalk for each port can be extracted by analyzing the table. Here, we find the largest isolation ratio is 14.4 dB between ports 2 and 3 (i.e., $\mathrm{IR}_{23} = |S_{23}|^2/|S_{32}|^2$), while the smallest isolation ratio is 2.5 dB between ports 1 and 6 (i.e., $\mathrm{IR}_{61} = |S_{16}|^2/|S_{61}|^2$). The insertion losses along the forward circulating path range from 10.1 to 14.3 dB, which is similar to what was measured in the 4-port device, and can be reduced by shortening the length of the Ce:YIG cladding above the bus waveguides. Overall, a better device performance can be achieved by aligning the resonances with better fabrication accuracy or a separate thermal tuner.

Table 3. Experimental Transmittance Data [dB] of the 6-Port Circulator at the Working Wavelength $\lambda = 1557.6$ nm

		Input Port					
		1	**2**	**3**	**4**	**5**	**6**
Output Port	**1**	–	-22.5	–	–	–	**-10.1**
	2	**-11.2**	–	-26.5	–	-20.4	–
	3	–	**-12.1**	–	-15.5	–	-29.3
	4	–	–	**-11.3**	–	-23.5	–
	5	–	-23.0	–	**-12.0**	–	-27.0
	6	-12.6	–	-30.3	–	**-14.3**	–

6. CONCLUSIONS

In conclusion, we have demonstrated, for the first time, to the best of our knowledge, a microring-based optical circulator that greatly shrinks the footprint of the device when compared to previous MZI-based circulators. The device uses an integrated electromagnet instead of conventional permanent magnets and can be easily reconfigured to select the direction of circulation, which may lead to new applications in sensing, data centers, and telecommunications. Finally, the device architecture we have proposed can be scaled to circulators with an arbitrary number of ports and multiple operating configurations. We demonstrate a 6-port circulator with up to 14.4 dB of isolation as a proof of concept. This scalability combined with a sub-nanosecond switching time could pave the way for novel optical switching and routing technologies.

Funding. Air Force Small Business Innovation Research (SBIR) (FA8650-16-C-1758); National Science Foundation (NSF) (CNS-0960316).

Acknowledgment. The authors also thank Jon Peters, Michael Davenport, and Tin Komljenovic from the University of California Santa Barbara, and Fabrizio Di Pasquale from Scuola Sant'Anna of Pisa (Italy) for the insightful advice and helpful discussions. D.H. also acknowledges the NSF GRFP for support.

[†]These authors contributed equally to this work.

See Supplement 1 for supporting content.

REFERENCES

1. D. Jalas, A. Petrov, M. Eich, W. Freude, S. Fan, Z. Yu, R. Baets, M. Popovic, A. Melloni, J. D. Joannopoulos, and M. Vanwolleghem, "What is—and what is not—an optical isolator," Nat. Photonics **7**, 579–582 (2013).
2. D. Dai and J. E. Bowers, "Silicon-based on-chip multiplexing technologies and devices for Peta-bit optical interconnects," Nanophotonics **3**, 283–311 (2014).
3. P. Pintus, N. Andriolli, F. Di Pasquale, and J. E. Bowers, "Bidirectional crosstalk and back-reflection free WDM active optical interconnects," IEEE Photon. Technol. Lett. **25**, 1973–1976 (2013).
4. K. Tai, B. Chang, J. Chen, C. H. Mao, T. Ducellier, J. Xie, L. Mao, and J. Wheeldon, "Wavelength-interleaving bidirectional circulators," IEEE Photon. Technol. Lett. **13**, 320–322 (2001).
5. H. Krishnaswamy and N. Reikarimian, "Magnetic-free non-reciprocity based on staggered commutation," Nat. Commun. **7**, 11217 (2016).
6. B. Lee and Y. Jeong, *Interrogation Techniques for Fiber Grating Sensors and the Theory of Fiber Gratings* (Marcel Dekker, 2002).
7. H. Lira, Z. Yu, S. Fan, and M. Lipson, "Electrically driven nonreciprocity induced by interband photonic transition on a silicon chip," Phys. Rev. Lett. **109**, 033901 (2012).
8. Z. Yu and S. Fan, "Complete optical isolation created by indirect interband photonic transitions," Nat. Photonics **3**, 91–94 (2009).
9. L. D. Tzuang, K. Fang, P. Nussenzveig, S. Fan, and M. Lipson, "Non-reciprocal phase shift induced by an effective magnetic flux for light," Nat. Photonics **8**, 701–705 (2014).
10. M. J. Heck, S. Srinivasan, M. L. Davenport, and J. E. Bowers, "Integrated microwave photonic isolators: theory, experimental realization and appli-

cation in a unidirectional ring mode-locked laser diode," Photonics **2**, 957–968 (2015).
11. Y. Yang, C. Galland, Y. Liu, K. Tan, R. Ding, Q. Li, K. Bergman, T. Baehr-Jones, and M. Hochberg, "Experimental demonstration of broadband Lorentz non-reciprocity in an integrable photonic architecture based on Mach–Zehnder modulators," Opt. Express **22**, 17409–17422 (2014).
12. C. R. Doerr, N. Dupuis, and L. Zhang, "Optical isolator using two tandem phase modulators," Opt. Lett. **36**, 4293–4295 (2011).
13. C. R. Doerr, L. Chen, and D. Vermeulen, "Silicon photonics broadband modulation-based isolator," Opt. Express **22**, 4493–4498 (2014).
14. C. G. Poulton, R. Pant, A. Byrnes, S. Fan, M. J. Steel, and B. J. Eggleton, "Design for broadband on-chip isolator using stimulated Brillouin scattering in dispersion-engineered chalcogenide waveguides," Opt. Express. **20**, 21235–21246 (2012).
15. C. H. Dong, Z. Shen, C. L. Zou, Y. L. Zhang, W. Fu, and G. C. Guo, "Brillouin-scattering-induced transparency and non-reciprocal light storage," Nat. Commun. **6**, 6193 (2015).
16. L. Fan, J. Wang, L. T. Varghese, H. Shen, B. Niu, Y. Xuan, A. M. Weiner, and M. Qi, "An all-silicon passive optical diode," Science **335**, 447–450 (2012).
17. L. Liu, J. Dong, D. Gao, A. Zheng, and X. Zhang, "On-chip passive three-port circuit of all-optical ordered-route transmission," Sci. Rep. **5**, 10190 (2015).
18. Y. Shi, Z. Yu, and S. Fan, "Limitations of nonlinear optical isolators due to dynamic reciprocity," Nat. Photonics **9**, 388–392 (2015).
19. B. J. Stadler and T. Mizumoto, "Integrated magneto-optical materials and isolators: a review," IEEE Photon. J. **6**, 1–15 (2014).
20. L. Bi, J. Hu, P. Jiang, D. H. Kim, G. F. Dionne, L. C. Kimerling, and C. A. Ross, "On-chip optical isolation in monolithically integrated non-reciprocal optical resonators," Nat. Photonics **5**, 758–762 (2011).
21. X. Y. Sun, Q. Du, T. Goto, M. C. Onbasli, D. H. Kim, N. M. Aimon, J. Hu, and C. A. Ross, "Single-step deposition of cerium-substituted yttrium iron garnet for monolithic on-chip optical isolation," ACS Photon. **2**, 856–863 (2015).
22. A. D. Block, P. Dulal, B. J. Stadler, and N. C. Seaton, "Growth parameters of fully crystallized YIG, Bi:YIG, and Ce:YIG films with high Faraday rotations," IEEE Photon. J. **6**, 1–8 (2014).
23. T. Goto, Y. Eto, K. Kobayashi, Y. Haga, M. Inoue, and C. A. Ross, "Vacuum annealed cerium-substituted yttrium iron garnet films on non-garnet substrates for integrated optical circuits," J. Appl. Phys. **113**, 17A939 (2013).
24. D. Liang, G. Roelkens, R. Baets, and J. E. Bowers, "Hybrid integrated platforms for silicon photonics," Materials **3**, 1782–1802 (2010).
25. M. J. Heck, J. F. Bauters, M. L. Davenport, J. K. Doylend, S. Jain, G. Kurczveil, S. Srinivasan, Y. Tang, and J. E. Bowers, "Hybrid silicon photonic integrated circuit technology," IEEE J. Sel. Top. Quantum Electron. **19**, 6100117 (2013).
26. T. Komljenovic, M. Davenport, J. Hulme, A. Y. Liu, C. T. Santis, A. Spott, S. Srinivasan, E. J. Stanton, C. Zhang, and J. E. Bowers, "Heterogeneous silicon photonic integrated circuits," J. Lightwave Technol. **34**, 20–35 (2016).
27. Y. Shoji, T. Mizumoto, H. Yokoi, I. W. Hseih, and R. M. Osgood, Jr., "Magneto-optical isolator with silicon waveguides fabricated by direct bonding," Appl. Phys. Lett. **92**, 071117 (2008).
28. Y. Shoji, Y. Shirato, and T. Mizumoto, "Silicon Mach–Zehnder interferometer optical isolator having 8 nm bandwidth for over 20 dB isolation," J. Appl. Phys. **53**, 022202 (2014).
29. Y. Shoji, M. Ito, Y. Shirato, and T. Mizumoto, "MZI optical isolator with Si-wire waveguides by surface-activated direct bonding," Opt. Express **20**, 18440–18448 (2012).
30. Y. Shoji, K. Miura, and T. Mizumoto, "Optical nonreciprocal devices based on magneto-optical phase shift in silicon photonics," J. Opt. **18**, 013001 (2015).
31. K. Mitsuya, Y. Shoji, and T. Mizumoto, "Demonstration of a silicon waveguide optical circulator," IEEE Photon. Technol. Lett. **25**, 721–723 (2013).
32. S. Ghosh, S. Keyvaninia, W. Van Roy, T. Mizumoto, G. Roelkens, and R. Baets, "Adhesively bonded Ce:YIG/SOI integrated optical circulator," Opt. Lett. **38**, 965–967 (2013).
33. S. Ghosh, S. Keyvaninia, Y. Shirato, T. Mizumoto, G. Roelkens, and R. Baets, "Optical isolator for TE polarized light realized by adhesive bonding of Ce:YIG on silicon-on-insulator waveguide circuits," IEEE Photon. J. **5**, 6601108 (2013).
34. M. C. Tien, T. Mizumoto, P. Pintus, H. Kroemer, and J. E. Bowers, "Silicon ring isolators with bonded nonreciprocal magneto-optic garnets," Opt. Express **19**, 11740–11745 (2011).
35. P. Pintus, F. Di Pasquale, and J. E. Bowers, "Integrated TE and TM optical circulators on ultra-low-loss silicon nitride platform," Opt. Express **21**, 5041–5052 (2013).
36. M. Yanaga, Y. Shoji, Y. Takamura, S. Nakagawa, and T. Mizumoto, "Compact magnetooptical isolator with cobalt ferrite on silicon photonic circuits," Appl. Phys. Express **8**, 082201 (2015).
37. D. Huang, P. Pintus, C. Zhong, Y. Shoji, T. Mizumoto, and J. E. Bowers, "Silicon microring isolator with large optical isolation and low loss," in *Optical Fiber Communication Conference* (Optical Society of America, 2016), paper Th1K-2.
38. D. Huang, P. Pintus, C. Zhong, Y. Shoji, T. Mizumoto, and J. E. Bowers, "Electrically driven and thermally tunable integrated optical isolators for silicon photonics," IEEE J. Sel. Top. Quantum Electron. **22**, 4403408 (2016).
39. M. Levy, R. M. Osgood, H. Hegde, F. J. Cadieu, R. Wolfe, and V. J. Fratello, "Integrated optical isolators with sputter-deposited thin-film magnets," IEEE Photon. Technol. Lett. **8**, 903–905 (1996).
40. P. Pintus, M. C. Tien, and J. E. Bowers, "Design of magneto-optical ring isolator on SOI based on the finite-element method," IEEE Photon. Technol. Lett. **23**, 1670–1672 (2011).
41. P. Pintus, "Accurate vectorial finite element mode solver for magneto-optic and anisotropic waveguides," Opt. Express **22**, 15737–15756 (2014).
42. K. Furuya, T. Nemoto, K. Kato, Y. Shoji, and T. Mizumoto, "Athermal operation of a waveguide optical isolator based on canceling phase deviations in a Mach–Zehnder interferometer," J. Lightwave Technol. **34**, 1699–1705 (2016).
43. P. Pintus, D. Huang, C. Zhang, Y. Shoji, T. Mizumoto, and J. E. Bowers, "Novel nonreciprocal devices with integrated electromagnet for silicon photonics," in *European Conference on Optical Communication* (2016).
44. K. Padmaraji and K. Bergman, "Resolving the thermal challenges for silicon microring resonator devices," Nanophotonics **3**, 269–281 (2014).
45. I. Tudosa, C. Stamm, A. B. Kashuba, F. King, H. C. Siegmann, J. Stöhr, G. Ju, B. Lu, and D. Weller, "The ultimate speed of magnetic switching in granular recording media," Nature **428**, 831–833 (2004).
46. P. Pintus, P. Contu, P. G. Raponi, I. Cerutti, and N. Andriolli, "Silicon-based all-optical multi microring network-on-chip," Opt. Lett. **39**, 797–800 (2014).